2026 IEEE International Conference on Robotics and Automation (ICRA 2026)
June 1-5, 2026. Vienna, Austria

Hybrid Model-learning Decoupled Control for Tendon-driven Multi-segment Continuum Robotic Bronchoscope

Ming-Yang Zhang, Zhen Li, Qiang Ye, Pan Fu, Yu-Peng Zhai, Han Ren,
Yawen Deng, Chao Guo, Wenhao He*, Gui-Bin Bian*

***Abstract*— Flexible tendon-driven multi-segment robotic bronchoscopes can reach peripheral lung regions for minimally invasive diagnosis and therapy. However, long tendon transmissions introduce friction, elasticity, and backlash, which couple the motion of adjacent segments and reduce operational accuracy and safety. This paper proposes a hybrid model-learning decoupled control framework for a two-segment bronchoscope that explicitly cancels distal-to-proximal coupling while compensating transmission disturbances. The method learns online a pose-dependent coupling map from synchronized encoder and electromagnetic measurements and uses it for feedforward cancellation in the proximal channel. In addition, an adaptive disturbance compensation module estimates per-tendon compliance and backlash to correct stretch and dead-zone effects. A two-segment tendon-driven robotic bronchoscope platform demonstrated a substantial reduction in proximal drift during distal actuation. At a 90° distal bend, the mean proximal coupling angle was 5.84°. Compared with the most commonly used piecewise constant curvature model baseline, the proposed controller achieved stronger motion decoupling, reducing the coupling rate by 86.47%, thereby enabling more precise bronchoscopic manipulation in anatomically constrained environments.**

I. INTRODUCTION

A. Background

Lung cancer is the leading cause of cancer mortality [1]. Flexible continuum robotic bronchoscopes have emerged as a promising tool for minimally invasive lung interventions, offering the ability to navigate deep into the bronchial tree while minimizing patient trauma [2]. An overview of the robotic bronchoscope and clinical scenario is shown in Fig. 1. Unlike rigid instruments, tendon-driven continuum robots can provide superior maneuverability in the narrow, tortuous airways of the lungs [3]. Robotic bronchoscope overcomes the limitation of conventional bronchoscopes, which cannot reach peripheral lung regions [4]. Recent robotic bronchoscopy and related endoscopic platforms employ single- or multi-segment continuum architectures [5]. Compared with single-segment designs, multi-segment robots provide greater distal dexterity and adaptability in tortuous airways [6]. However, multi-segment tendon-driven robots still face major challenges in precise control. Long and elastic drive tendons introduce strong nonlinear effects, such as friction, backlash, and hysteresis, and they cause coupling between segments [7], [8]. Decoupled control can maximize the advantages of the multi-segment continuum robot.

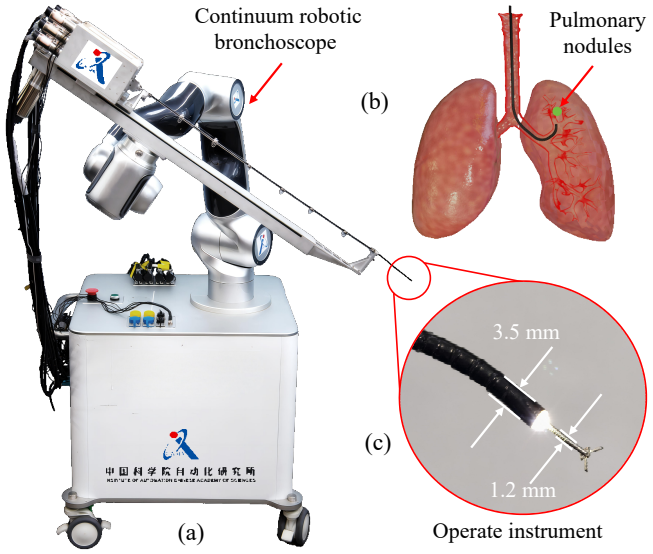

Fig. 1. Overview of the robotic bronchoscope and clinical scenario. (a) Tendon-driven continuum robotic bronchoscope. (b) Schematic diagram of bronchoscopic sampling and examination of pulmonary nodules. (c) Curved section at the end of the robotic bronchoscope and inspection instrument.

B. Related Studies

In recent years, decoupling methods have been commonly grouped as mechanical, model-based and learning-based. Russo [9] *et al.* proposed helical tendon routing

*This research is supported by the National Key Research and Development Program of China (Grant 2024YFB4708800, 2025YFC2428700), the National Natural Science Foundation of China (Grant 62525311), the Beijing Municipal Natural Science Foundation (Grant L258029, L252002, L232038).

Corresponding author: Gui-Bin Bian and Wenhao He.

Ming-Yang Zhang and Wenhao He are with the State Key Laboratory of Multimodal Artificial Intelligence Systems, Institute of Automation, Chinese Academy of Sciences, Beijing, 100190, China, and also with the School of Artificial Intelligence, University of Chinese Academy of Sciences, Beijing 100049, China. Zhangmingyang2024@ia.ac.cn; wenhao.he@ia.ac.cn

Zhen Li is with the School of Electronic and Information Engineering, Tongji University, Shanghai, 200092, China, and Institute of Automation, Chinese Academy of Sciences, Beijing, 100190, China. zhen.li@ia.ac.cn

Qiang Ye, Pan Fu, Han Ren, Yawen Deng and Gui-Bin Bian are with the State Key Laboratory of Multimodal Artificial Intelligence Systems, Institute of Automation, Chinese Academy of Sciences, Beijing, 100190, China. qiang.ye@ia.ac.cn; 3120235660@bit.edu.cn; renhan.casia@gmail.com; dengyawen@foxmail.com; guibin.bian@ia.ac.cn

Yu-Peng Zhai is with the College of Integrated Circuits, Taiyuan University of Technology, Taiyuan, 030024, China. yvpeng.zhai@gmail.com

Chao Guo is with the Department of Thoracic Surgery, Peking Union Medical College Hospital, Peking Union Medical College and Chinese Academy of Medical Sciences, Beijing, 100730, China. guochao@pumch.cn

to physically decouple backbone segments compared with conventional straight routing. Xu [10] *et al.* introduced a variable-pitch flexible-screw–driven architecture that realizes inter-section motion decoupling on hardware. However, such mechanical schemes often increase structural complexity and constrain miniaturization. On the modeling side, Zeng [8] *et al.* derived a coupled-mechanics analysis for two-segment notched robots to guide decoupled design, and further presented a model-based design optimization built on a non-constant-curvature Euler–Bernoulli moment–curvature mechanics model that minimizes inter-segment coupling [11]. Piecewise constant curvature (PCC) based formulations remain popular for efficient multi-segment control, because they are easy to compute. Fischer [12] *et al.* demonstrated dynamic task-space control under a PCC assumption. However, model-based methods have difficulty capturing the nonlinear behavior of long, compliant tendons , which reduces accuracy [13]. At the learning level, Hu [14] *et al.* realized decoupled bending–elongation patterns with a hybrid-driven modular continuum robot. Zhao [15] *et al.* designed a controller that kinematically decouples bending and continuous rotation via optimization with online Jacobian correction. Nazeer [16] *et al.* incorporated continuum kinematic/dynamic priors into model-based reinforcement-learning (RL) to guide learning, enhancing training stability and convergence, while Thuruthel [17] *et al.* developed an online-learning, model-less feedback controller that achieved accurate positioning in unstructured environments. Wei [18] *et al.* proposed the Axis-Space RL framework, thereby isolating segment commands to assist decoupled control while reducing sample complexity. Nevertheless, many learning-based controllers suffer from limited data efficiency, requiring prohibitively large numbers of training samples or simulations to cover the robot's high-dimensional state space. In short, robust decoupled control of multi-segment tendon-driven bronchoscopes remains a challenging problem.

C. Contributions

This paper proposes a hybrid model-learning, lightweight decoupled control method for a tendon-driven two-segment continuum bronchoscope. The main contributions are: 1) An online identification–based feedforward decoupling architecture with adaptive tendon elasticity and backlash compensation was proposed, enabling real-time independent control of proximal and distal segments under nonlinear tendon disturbances. 2) An electromagnetic (EM) guided, safety-constrained, closed-loop controller is developed that fuses task-space feedback with curvature, tension, and actuation-rate limits, yielding stable distal-tip control and robust operation in confined airways. 3) The construction of an experimental platform and comprehensive hardware validation, demonstrating the effectiveness and reliability of the proposed method.

II. Modeling and Online Identification

A. Kinematics & Actuation-Space Mapping

As shown in Fig. 2, two serial segments are indexed by $j \in \{1, 2\}$, where $j = 1$ denotes the proximal segment and $j = 2$ denotes the distal segment. Each segment has bending magnitude θ_j and bending plane angle α_j, collected as

$$x_j = \begin{bmatrix} \theta_j \\ \alpha_j \end{bmatrix} \in \mathbb{R}^2. \tag{1}$$

A tri-tendon layout is used on each segment with tendons indexed by $i \in \{1, 2, 3\}$ and cross-section radius $r > 0$. The tendon anchor angles on the proximal segment are

$$\{\phi_{1,i}\}_{i=1}^{3} = \Big\{0,\ \tfrac{2\pi}{3},\ \tfrac{4\pi}{3}\Big\}, \tag{2}$$

and on the distal segment are

$$\{\phi_{2,i}\}_{i=1}^{3} = \Big\{\tfrac{\pi}{3},\ \pi,\ \tfrac{5\pi}{3}\Big\}. \tag{3}$$

The nominal tendon-length increment for tendon i on segment j generated by the segment configuration x_j is defined as

$$\Delta l_{j,i}^{\mathrm{ref}} = r\,\theta_j\,\cos\big(\alpha_j + \phi_{j,i}\big). \tag{4}$$

Define the stacked nominal tendon increment

$$\begin{aligned} &\Delta \mathbf{l}^{\mathrm{ref}} = \begin{bmatrix} \Delta \mathbf{l}_1^{\mathrm{ref}} \\ \Delta \mathbf{l}_2^{\mathrm{ref}} \end{bmatrix} \in \mathbb{R}^6, \\ &\Delta \mathbf{l}_j^{\mathrm{ref}} = \begin{bmatrix} \Delta l_{j,1}^{\mathrm{ref}} & \Delta l_{j,2}^{\mathrm{ref}} & \Delta l_{j,3}^{\mathrm{ref}} \end{bmatrix}^{\top} \in \mathbb{R}^3, \quad j \in \{1, 2\}. \end{aligned} \tag{5}$$

PCC forward kinematics provide the tip pose as a function of x_1 and x_2. PCC inverse kinematics produce segment references $x_1^\star$ and $x_2^\star$ from a desired tip pose. In this work, the nominal tendon increments are computed directly from (4) for each segment.

B. Adaptive Disturbance Compensation (ADC)

For brevity, the combined elastic-and-backlash compensation term is referred to as adaptive disturbance compensation (ADC). Let $\boldsymbol{\tau} = [\tau_1, \ldots, \tau_6]^{\top} \in \mathbb{R}^6$ denote tendon tensions and let $\Delta \mathbf{l}_e \in \mathbb{R}^6$ denote the elastic stretch to be compensated. Let $K = \mathrm{diag}(\kappa_1, \ldots, \kappa_6)$ be the diagonal compliance matrix where $\kappa_i > 0$ is the compliance of tendon i. The elastic model is

$$\Delta \mathbf{l}_e = K\,\boldsymbol{\tau}. \tag{6}$$

Let t index the control step. Let $\Delta l_{i,t}^{\mathrm{meas}}$ be the measured length increment of tendon i from encoders and let $\Delta l_{i,t}^{\mathrm{ref}}$ be the nominal increment from the kinematic mapping. Define $y_t^{(i)} = \Delta l_{i,t}^{\mathrm{meas}} - \Delta l_{i,t}^{\mathrm{ref}}$ and $\varphi_t = \tau_{i,t}$. The scalar recursive least squares (RLS) identifies κ_i online with forgetting factor $\lambda \in (0, 1]$:

$$\begin{aligned} &G_t = \frac{P_{t-1}\varphi_t}{\lambda + \varphi_t^{\top} P_{t-1}\varphi_t}, \quad \hat{\kappa}_{i,t} = \hat{\kappa}_{i,t-1} + G_t\big(y_t - \varphi_t^{\top}\hat{\kappa}_{i,t-1}\big), \\ &P_t = \lambda^{-1}\big(I - G_t\varphi_t^{\top}\big)P_{t-1}, \end{aligned} \tag{7}$$

where $\hat{\kappa}_{i,t}$ is the online estimate of the compliance parameter of tendon i, P_t is the covariance matrix, I is the identity matrix, and G_t is the RLS gain.

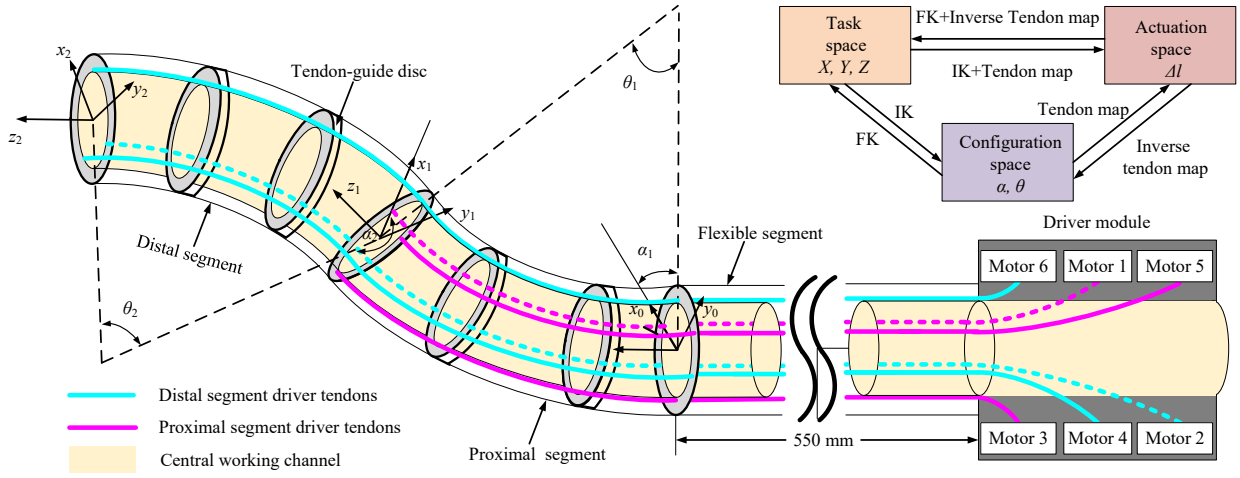

Fig. 2. Schematic of the kinematics for a two-segment tendon-driven continuum robotic bronchoscope.

Let $\Delta l_i^{\mathrm{cmd}}$ be the commanded increment for tendon i and let $\Delta l_i^{\mathrm{eff}}$ be the effective increment after backlash compensation. Let $d_i \geq 0$ be the backlash magnitude for tendon i. Let $\dot{l}_i$ be the tendon length rate and let $\sigma(\dot{l}) = \tanh(\dot{l}/v_0)$ be a smooth sign surrogate with scale $v_0 > 0$. The backlash model is

$$\Delta l_i^{\mathrm{eff}} = \Delta l_i^{\mathrm{cmd}} + d_i\, \sigma(\dot{l}_i). \tag{8}$$

Define the instantaneous mismatch

$$\varepsilon_{i,t} = \Delta l_{i,t}^{\mathrm{meas}} - \Delta l_{i,t}^{\mathrm{ref}} - \kappa_i \tau_{i,t} - d_i \sigma(\dot{l}_{i,t}), \tag{9}$$

and update d_i by a projected gradient with step size $\eta > 0$ and upper bound $d_{\max} > 0$

$$d_i \leftarrow \Pi_{[0,d_{\max}]}\Big(d_i - \eta\, \sigma(\dot{l}_{i,t})\, \varepsilon_{i,t}\Big), \tag{10}$$

where $\Pi_{[0,d_{\max}]}$ denotes projection onto the closed interval $[0, d_{\max}]$.

Let $\Delta \mathbf{l}_{\mathrm{dz}} \in \mathbb{R}^6$ stack the backlash offsets with $(\Delta \mathbf{l}_{\mathrm{dz}})_i = d_i\, \sigma(\dot{l}_i)$. The compensated actuator increment is

$$\Delta \mathbf{l}_{\mathrm{ADC}} = \Delta \mathbf{l}^{\mathrm{ref}} + \Delta \mathbf{l}_e + \Delta \mathbf{l}_{\mathrm{dz}}, \tag{11}$$

where $\Delta \mathbf{l}^{\mathrm{ref}} \in \mathbb{R}^6$ is the nominal geometric increment produced by the kinematic mapping.

C. Online Learning of Distal-to-Proximal Coupling

Distal tendons traverse the proximal segment, hence distal actuation induces passive changes in the proximal tendons. Let $\Delta \mathbf{l}_1^{\mathrm{cpl}} \in \mathbb{R}^3$ denote the passive length increment of the three proximal tendons caused by distal actuation, let $\Delta \mathbf{l}_2 \in \mathbb{R}^3$ denote the distal tendon increment, let $x_2 = [\theta_2, \alpha_2]^\top$ denote the distal segment configuration, and let $\mathbf{v}$ denote noise and unmodeled effects. A local length-domain coupling is modeled as

$$\Delta \mathbf{l}_1^{\mathrm{cpl}} \approx \mathbf{C}_{12}(x_2)\, \Delta \mathbf{l}_2 + \mathbf{v}, \qquad \mathbf{C}_{12}(x_2) \in \mathbb{R}^{3\times 3}. \tag{12}$$

In general, the coupling term $\mathbf{C}_{12}(x_2)$ is nonlinear because it depends on tendon routing, distributed friction, and structural compliance. However, within the bounded operating range considered in this study, the measured proximal disturbance varies smoothly with the distal configuration. Therefore, for real-time control, we approximate this effect using a low-order local parameterization that is compact, interpretable, and efficient to update online.

Define the pose feature vector $\psi(x_2) = [1,\ \theta_2,\ \cos\alpha_2,\ \sin\alpha_2]^\top \in \mathbb{R}^4$. Parameterize

$$\hat{\mathbf{C}}_{12}(x_2) = W_0 + W_\theta\, \theta_2 + W_c\, \cos\alpha_2 + W_s\, \sin\alpha_2, \tag{13}$$

where $W_0,\ W_\theta,\ W_c,\ W_s \in \mathbb{R}^{3\times 3}$ are updated online by block RLS using streaming pairs $\Delta \mathbf{l}_2^{\mathrm{ref}}$ as regressors and $\Delta \mathbf{l}_1^{\mathrm{meas}} - \Delta \mathbf{l}_1^{\mathrm{ref}}$ as targets. The distal configuration x_2 is obtained from EM tracking and geometry.

D. Decoupling Metric and Safety Constraints

Consider a distal-only motion test where the proximal nominal increment is zero, $\Delta \mathbf{l}_1^{\mathrm{ref}} = \mathbf{0}$. Let $p_1(t) \in \mathbb{R}^3$ denote the proximal segment endpoint position at time t. Let $\mathcal{T}$ be a time window and $|\mathcal{T}|$ its cardinality. The distal-to-proximal decoupling index is defined as

$$\mathrm{DI}_{12} = \sqrt{\frac{1}{|\mathcal{T}|} \sum_{t\in\mathcal{T}} \big\| p_1(t) - p_1(t_0) \big\|_2^2}. \tag{14}$$

where t_0 is the window start and $\|\cdot\|_2$ is the Euclidean norm. The position $p_1(t)$ is computed from proximal tendon lengths through forward kinematics or from an EM sensor.

Safety envelopes enforce bounded kinematics and actuation. Let θ_j be the bending magnitude of segment j and $\theta_{j,\max}$ its limit. Let $\boldsymbol{\tau} \in \mathbb{R}^6$ be the tendon tension vector from load cells or current-based estimators and let $\tau_{\max}$ be the tension limit. Let $\mathbf{u} \in \mathbb{R}^6$ be the actuator command increment in tendon space and let $\Delta \mathbf{u}$ be its step-to-step change. The controller respects

$$\begin{aligned} |\theta_j| \leq \theta_{j,\max}, \quad \|\boldsymbol{\tau}\|_\infty \leq \tau_{\max}, \\ \|\mathbf{u}\|_\infty \leq u_{\max}, \quad \|\Delta \mathbf{u}\|_\infty \leq \Delta u_{\max}. \end{aligned} \tag{15}$$

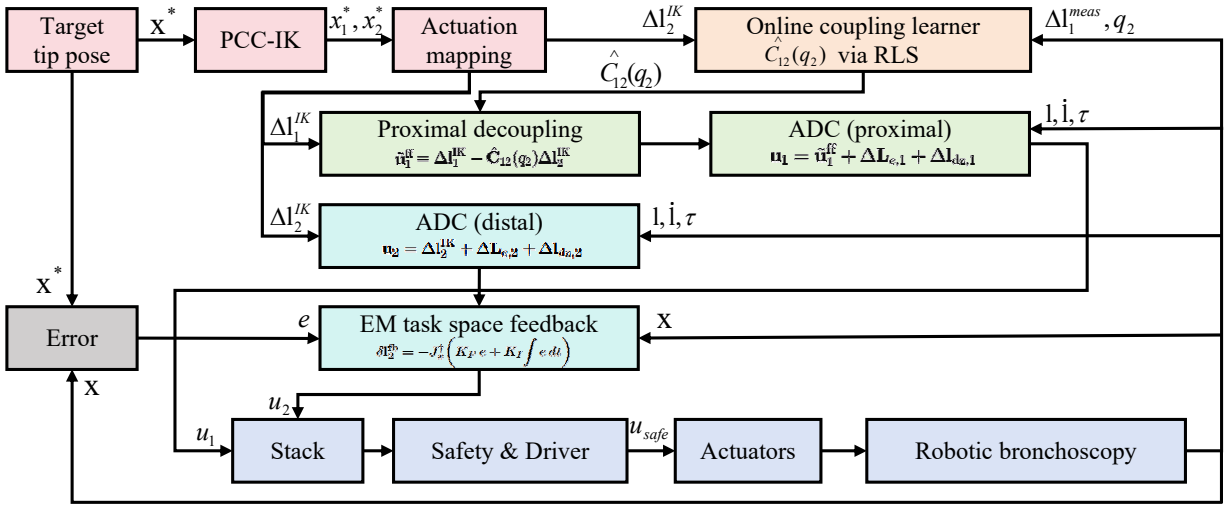

Fig. 3. Control block diagram of the proposed hybrid decoupled controller for a two-segment tendon-driven continuum bronchoscope.

All model parameters are updated online from synchronized encoder increments, distal pose from EM tracking, and optional tendon tensions.

III. Lightweight Decoupled Controller

A. Hierarchical Task Split and Nominal References

The proximal segment provides airway alignment and baseline guidance. The distal segment performs precise tip positioning. Given desired segment references $x_1^\star$ and $x_2^\star$ from PCC inverse kinematics, the nominal tendon increments are

$$\Delta \mathbf{l}_1^{\mathrm{ref}} = \mathcal{M}_1(x_1^\star), \qquad \Delta \mathbf{l}_2^{\mathrm{ref}} = \mathcal{M}_2(x_2^\star), \tag{16}$$

where $\mathcal{M}_j(\cdot)$ denotes the tri-tendon kinematic map defined by (4) for segment j.

B. Feedforward Decoupling in the Proximal Channel and ADC

Let $\mathbf{u}_1 \in \mathbb{R}^3$ denote the proximal actuator command in tendon space and let $\mathbf{u}_2 \in \mathbb{R}^3$ denote the distal actuator command. Let $\Delta \mathbf{l}_j^{\mathrm{ref}} \in \mathbb{R}^3$ be the nominal tendon increment of segment j from kinematics, with $j = 1$ proximal and $j = 2$ distal. Let $x_2 = [\theta_2, \alpha_2]^\top$ be the distal segment configuration. Let $\hat{\mathbf{C}}_{12}(x_2) \in \mathbb{R}^{3\times 3}$ be the online learned distal-to-proximal coupling map. Let $\Delta \mathbf{l}_{e,j} \in \mathbb{R}^3$ and $\Delta \mathbf{l}_{\mathrm{dz},j} \in \mathbb{R}^3$ be the elastic and backlash compensations for segment j. The feedforward decoupling with adaptive compensation is

$$\mathbf{u}_1 = \Delta \mathbf{l}_1^{\mathrm{ref}} - \hat{\mathbf{C}}_{12}(x_2)\, \Delta \mathbf{l}_2^{\mathrm{ref}} + \Delta \mathbf{l}_{e,1} + \Delta \mathbf{l}_{\mathrm{dz},1}, \tag{17}$$

$$\mathbf{u}_2 = \Delta \mathbf{l}_2^{\mathrm{ref}} + \Delta \mathbf{l}_{e,2} + \Delta \mathbf{l}_{\mathrm{dz},2}. \tag{18}$$

Let $\Pi_{\mathcal{U}}$ denote the safety projector that enforces actuation, rate, tension and curvature limits. The stacked command is

$$\mathbf{u} \;=\; \Pi_{\mathcal{U}}\!\left(\begin{bmatrix}\mathbf{u}_1\\ \mathbf{u}_2\end{bmatrix}\right). \tag{19}$$

First-order drift bound. Let $\tilde{\mathbf{C}}_{12} = \mathbf{C}_{12} - \hat{\mathbf{C}}_{12}$ be the coupling estimation error, where $\mathbf{C}_{12}$ is the true coupling. Let $J_{l\mapsto p_1} \in \mathbb{R}^{3\times 3}$ be the proximal tendon-to-endpoint Jacobian that maps proximal tendon increments to the proximal endpoint displacement. Let $\Delta p_1 \in \mathbb{R}^3$ be that endpoint displacement. For distal-only motion with $\Delta \mathbf{l}_1^{\mathrm{ref}} = \mathbf{0}$

$$\Delta p_1 \;\approx\; J_{l\mapsto p_1}\left(\tilde{\mathbf{C}}_{12}\, \Delta \mathbf{l}_2^{\mathrm{ref}} + \Delta \mathbf{l}_{e,1} + \Delta \mathbf{l}_{\mathrm{dz},1}\right), \tag{20}$$

which implies the norm bound

$$\|\Delta p_1\| \;\le\; \|J_{l\mapsto p_1}\|\left(\|\tilde{\mathbf{C}}_{12}\|\,\|\Delta \mathbf{l}_2^{\mathrm{ref}}\| + \|\Delta \mathbf{l}_{e,1}\| + \|\Delta \mathbf{l}_{\mathrm{dz},1}\|\right). \tag{21}$$

Here $\|\cdot\|$ denotes the induced matrix norm or Euclidean norm as appropriate.

C. EM Feedback and Real-Time Loop

EM tracking supplies the measured distal tip pose $\mathbf{x} \in \mathbb{R}^3$. The desired tip pose is $\mathbf{x}^\star \in \mathbb{R}^3$. The tip pose error is $e = \mathbf{x}^\star - \mathbf{x}$. The task-space Jacobian $J_x \in \mathbb{R}^{m\times 3}$ maps distal tendon increments to tip velocity at the operating point. The symbol $J_x^\dagger$ denotes a damped pseudoinverse of J_x used for numerical robustness. The matrices K_P and K_I are proportional and integral gain matrices in task space. The vector $\delta \mathbf{l}_2^{\mathrm{fb}} \in \mathbb{R}^3$ is a feedback increment in the distal tendon space and $\mathbf{u}_2 \in \mathbb{R}^3$ is the distal actuator command. A small-gain feedback is applied on the distal channel

$$\delta \mathbf{l}_2^{\mathrm{fb}} = -J_x^\dagger\left(K_P\, e + K_I \int e\, dt\right), \qquad \mathbf{u}_2 \leftarrow \mathbf{u}_2 + \delta \mathbf{l}_2^{\mathrm{fb}}. \tag{22}$$

Each control cycle performs the following sequence. Electromagnetic tracking and encoders are read and lightly filtered to obtain $\mathbf{x}$, $\mathbf{l}$, $\dot{\mathbf{l}}$ and the tendon tensions $\boldsymbol{\tau}$. Inverse kinematics provides segment references that yield the nominal tendon increments for both segments. Feedforward decoupling with adaptive compensation generates proximal and distal commands using (17) and (18). The feedback term (22) refines the distal command. A safety projection $\Pi_{\mathcal{U}}$

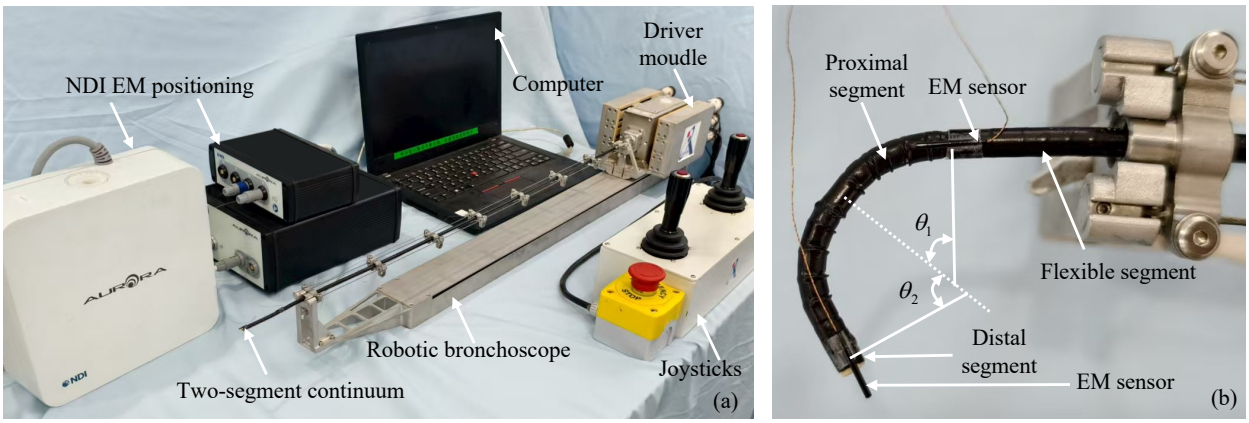

Fig. 4. Experimental platform. (a) Robotic bronchoscope system. (b) EM sensor arrangement on the proximal and distal segments for online coupling learning.

enforces the limits in (15) and produces the final actuator command. Motors are then actuated.

Online estimators are updated in the same cycle. Recursive least squares adjusts the elastic compliance parameters in the matrix K. A projected gradient step updates the backlash magnitudes d_i. The coupling map $\hat{\mathbf{C}}_{12}(x_2)$ is updated online as defined in Section II. As the identifiers converge, the closed loop reduces the distal-to-proximal decoupling index defined in (14). Fig. 3 shows the framework of the proposed hybrid decoupling controller.

IV. Experiments and Results Analysis

A. Experimental Setup

To evaluate the motion performance and decoupling efficacy of the proposed method, a continuum robotic bronchoscope prototype was built, and experiments were conducted on the platform shown in Fig. 4. The setup comprises the robotic bronchoscope and an EM tracker (NDI®, Canada; accuracy 0.7 mm). The actuation module provides six motorized drive axes (SMJ®, Japan) and integrates six in-line tension sensors (AUTODA®, China; accuracy 150 mN). Two joysticks independently command the bending magnitude and plane of the two continuum segments. The onboard controller reads the analog joystick signals, computes the kinematics of the two segments, and drives the motors accordingly.

Two EM sensors are mounted at the base and distal end of the continuum, and their position data are logged on a host computer to learn the proposed decoupling model. The tension sensors communicate via RS-485, and the EM tracker communicates via TCP/IP. The proposed method is verified in free state and restricted environments.

B. Free State Bending and Decoupled Capacity

To visually assess decoupling between the two continuum segments, the robot was fixed in free space to remove external contact and load. Independent commands were issued to the proximal and distal segments, and the non-actuated segment was held at zero command with no tension increment. Images were recorded at each steady configuration.

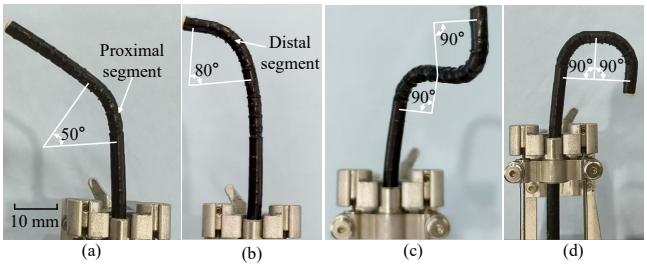

Fig. 5. Free state bending capacity of the two-segment continuum robotic bronchoscope. (a) The proximal segment bends while the distal segment remains stationary. (b) The distal segment bends while the proximal segment remains stationary. (c) The proximal and distal segments bend 90° in opposite directions. (d) The proximal and distal segments bend 90° in the same direction.

Fig. 5 presents the free-state decoupled behavior. Fig. 5(a) shows proximal-only bending with the distal segment stationary; the proximal forms a stable arc, and the distal exhibits no discernible co-motion in the same plane, indicating negligible influence. Fig. 5(b) shows distal-only bending with the proximal straight; when the distal reaches its target pose, the proximal position and orientation remain stable with no visible coupling drift, demonstrating effective decoupling. Fig. 5(c) shows both segments bending by about 90° in opposite directions without mutual interference. Fig. 5(d) shows both segments bending by about 90° in the same direction. The motions superimpose rather than pull each other, and the overall configuration remains smooth and continuous. These observations indicate that, in the free state, the controller achieves a clear separation between single-segment and two-segment actions. Whether one segment or both are actuated, the inactive segment remains at rest or shows only minimal residual displacement, confirming the effectiveness of the method.

To evaluate the decoupled controller and quantify proximal coupling induced by distal actuation, a contact-free free-state experiment was performed. The proximal segment was held at zero command, while the distal segment was varied on an evenly spaced grid: bend angle from 0° to 90° in 10°

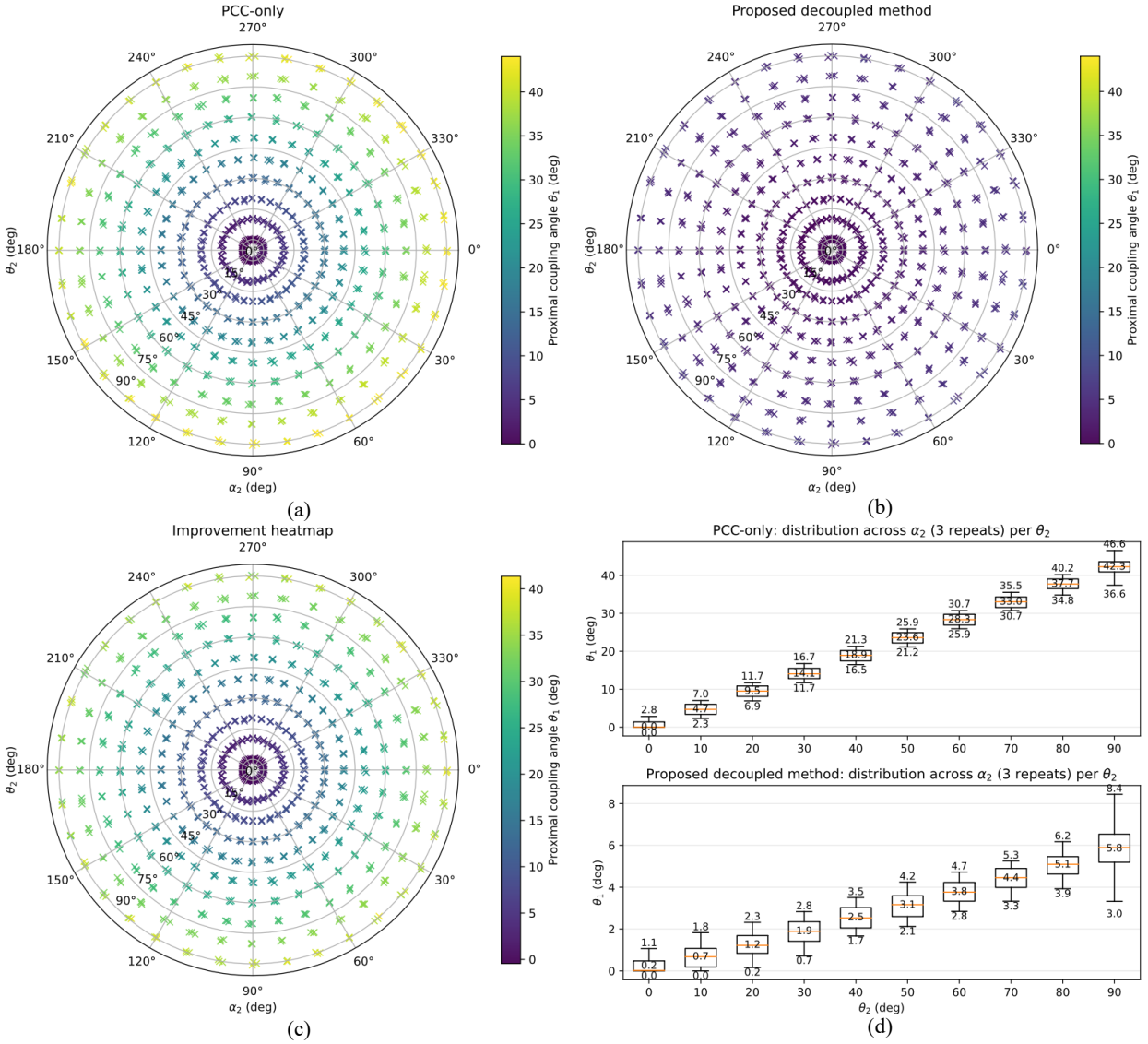

Fig. 6. Decoupling performance under distal actuation on a $10^\circ \times 10^\circ$ grid of rotation and bend angles, with three repeats per grid point. (a) Proximal segment coupling angle heatmap using the PCC-only controller: proximal segment coupling angle over the 10° rotation–bend grid. (b) Proximal segment coupling angle heatmap using the proposed decoupled controller: proximal segment coupling angle on the same 10° rotation–bend grid. (c) Improvement map: reduction in proximal segment coupling angle relative to PCC-only. (d) Box plots of proximal segment coupling angle versus distal bend angle, aggregating all rotation angles.

steps and rotation angle from 0° to 360° in 10° steps. Each grid point was held for 1-2 s to reach steady state, and EM tracked tip pose, actuator encoder length increments, and the tension of each tendon were recorded at 100 Hz. To remove batch effects, the PCC-only controller and the proposed decoupled controller were executed sequentially on the same grid. Each grid point was repeated three times to assess repeatability and statistical robustness. Curvature and tension safety limits were enforced throughout. Three EM sensors were deployed at the base, at the proximal tip, and at the distal tip. The proximal coupling angle was computed from the EM-measured poses using PCC kinematics, and the resulting statistics were used to construct the heatmaps and box plots.

Fig. 6 compares the proposed hybrid decoupling method with a conventional PCC controller [19] under distal actuation. Experiments were performed on a $10^\circ \times 10^\circ$ grid of rotation and bend angles with three repeats per grid point. Fig. 6(a) shows the proximal segment coupling angle heatmap for PCC-only. Fig. 6(b) presents the proposed method under the same grid and a shared color scale. Fig. 6(c) visualizes the improvement map as the difference between the two, with all heatmaps aggregating three repeats per point. Fig. 6(d) summarizes all rotation angles and repeats at each bend angle as two box plots, highlighting distribution shrinkage and changes in the mean level.

Table I lists each plot from Fig. 6 and provides the overall data analysis. As the distal bend increases, the proximal segment coupling angle rises monotonically. From 0° to 90°, the PCC mean increases from 0.66° to 42.19°. The proposed

TABLE I

COMPARISON TABLE OF EXPERIMENTAL RESULTS BETWEEN PCC AND THE PROPOSED DECOUPLED METHOD

θ_2 (deg)	PCC mean±std	Proposed mean±std	Improvement (deg)	Reduction (%)
0	0.66 ± 0.82	0.24 ± 0.29	0.43	—
10	4.70 ± 1.42	0.67 ± 0.50	4.03	85.66
20	9.43 ± 1.43	1.24 ± 0.52	8.20	86.91
30	14.17 ± 1.44	1.90 ± 0.53	12.28	86.61
40	18.81 ± 1.42	2.55 ± 0.53	16.26	86.45
50	23.56 ± 1.49	3.14 ± 0.56	20.42	86.66
60	28.32 ± 1.42	3.78 ± 0.53	24.54	86.65
70	32.98 ± 1.45	4.43 ± 0.49	28.55	86.56
80	37.74 ± 1.47	5.08 ± 0.54	32.67	86.55
90	42.19 ± 2.08	5.84 ± 1.12	36.35	86.15

method remains low from 0.24° to 5.84°. The absolute improvement grows with the bend and reaches 36.35° at 90°. The relative reduction is about 86% from 10° to 90°. The proposed method also yields a smaller standard deviation. At 90°, PCC is 2.08° while the proposed method is about 1.12°. These trends indicate monotonic coupling under PCC and effective decoupling with stable repeatability under the proposed method.

C. Demonstration of Decoupling Performance in Bronchial Model

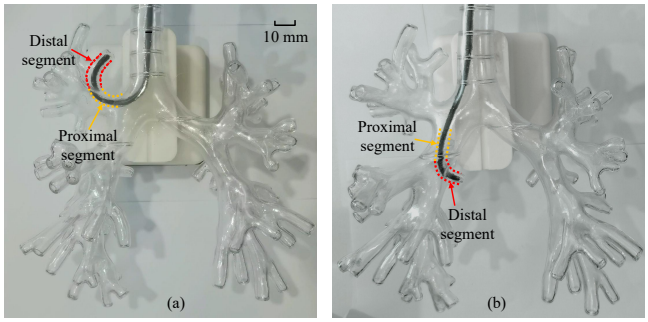

Fig. 7. Representative challenging maneuvers of the robotic bronchoscope in the bronchial model. (a) Two segments actuated cooperatively to enter the right upper lobe bronchus. (b) Distal-only bending to enter the right middle lobe bronchus.

To visually validate decoupled manipulation in anatomically constrained airways, experiments were conducted in a 1:1 scale 3D-printed model of the human bronchial tree. The lower lobe requires smaller bending angles so that the robotic bronchoscope can enter readily. Fig. 7 presents representative challenging maneuvers within the model. Fig. 7(a) shows access to the right upper lobe. With coordinated motion of both segments, the robot reaches the sharpest and most difficult region of the lung to enter. Fig. 7(b) shows entry into the right middle lobe. The distal segment negotiates a large-angle turn while the proximal segment exhibits only negligible coupled displacement, reducing contact with the bronchial wall. Overall, by coordinating the bend angles of the two continuum segments, the robot can reach arbitrary locations within the model, demonstrating effective decoupling and practical performance in the bronchial environment.

V. CONCLUSIONS AND FUTURE RESEARCH

This work proposed a lightweight hybrid model-learning decoupled control framework for a two-segment tendon-driven continuum bronchoscope. The approach uses PCC kinematics as prior structure, identifies distal to proximal coupling online for feedforward cancellation on the proximal channel, adds adaptive compensation for tendon elasticity and backlash, and closes the loop with low-gain EM task space feedback under safety constraints to form a stable loop. Free state sweeps and grid experiments show a monotonic and repeatable actuation to pose mapping, a marked reduction of proximal coupling during distal actuation, and robust tracking at large bends. At 90° the proximal coupling angle dropped from 42.19° to 5.84° with an improvement of 86.47%. This study provides a decoupling control method for multi-segment continuum robots. In the bronchial model demonstration, the two-segment continuum can reach any position through decoupling fit, which verifies the effectiveness of the proposed method in a confined environment. Future work will fuse preoperative CT based reconstructions with intraoperative EM or vision based navigation to achieve patient specific airway map registration and real time localization, thereby providing a high confidence environment model for robust path tracking.

REFERENCES

[1] F. Bray, M. Laversanne, H. Sung, J. Ferlay, R. L. Siegel, I. Soerjomataram, and A. Jemal, "Global cancer statistics 2022: Globocan estimates of incidence and mortality worldwide for 36 cancers in 185 countries," *CA: a cancer journal for clinicians*, vol. 74, no. 3, pp. 229–263, 2024.

[2] R. Paez, R. J. Lentz, J. D. Duke, J. K. Siemann, C. Salmon, G. J. Dahlberg, A. P. Ratwani, J. D. Casey, H. Chen, S.-C. Chen, *et al.*, "Robotic versus electromagnetic bronchoscopy for peripheral pulmonary lesions: A randomized trial (reliant)," *American Journal of Respiratory and Critical Care Medicine*, vol. 211, no. 9, pp. 1644–1651, 2025.

[3] P. E. Dupont, B. J. Nelson, M. Goldfarb, B. Hannaford, A. Menciassi, M. K. O'Malley, N. Simaan, P. Valdastri, and G.-Z. Yang, "A decade retrospective of medical robotics research from 2010 to 2020," *Science robotics*, vol. 6, no. 60, p. eabi8017, 2021.

[4] S. Murgu, A. C. Chen, C. R. Gilbert, D. H. Sterman, D. Pederson, S. Rafeq, B. Laxmanan, M. L. Schwiers, J. Connelly, H. L. Benz, *et al.*, "A prospective, multicenter evaluation of safety and diagnostic outcomes with robotic-assisted bronchoscopy: results of the transbronchial biopsy assisted by robot guidance in the evaluation of tumors of the lung (target) trial," *Chest*, vol. 168, no. 2, pp. 539–555, 2025.

[5] P. E. Dupont, N. Simaan, H. Choset, and C. Rucker, "Continuum robots for medical interventions," *Proceedings of the IEEE*, vol. 110, no. 7, pp. 847–870, 2022.
[6] H. Gao, X. Yang, X. Xiao, X. Zhu, T. Zhang, C. Hou, H. Liu, M. Q.-H. Meng, L. Sun, X. Zuo, *et al.*, "Transendoscopic flexible parallel continuum robotic mechanism for bimanual endoscopic submucosal dissection," *The International Journal of Robotics Research*, vol. 43, no. 3, pp. 281–304, 2024.
[7] Q. Gao, G. Ji, M. Sun, Y. Xiao, H. Rao, and Z. Sun, "Dynamic hysteresis compensation for tendon-sheath mechanism in flexible surgical robots without distal perception," *IEEE Transactions on Robotics*, vol. 41, pp. 3703–3721, 2025.
[8] W. Zeng, J. Yan, X. Huang, and S. S. Cheng, "Motion coupling analysis for the decoupled design of a two-segment notched continuum robot," in *2021 IEEE International Conference on Robotics and Automation (ICRA)*, pp. 7665–7671, IEEE, 2021.
[9] M. Russo, S. Wild, X. Dong, and D. Axinte, "Helical routing: Decoupling segments of tendon-driven continuum robots," *IEEE/ASME Transactions on Mechatronics*, vol. 30, no. 3, pp. 2257–2269, 2025.
[10] Y. Xu, D. Song, K. Zhang, and C. Shi, "Development of a variable-pitch flexible-screw-driven continuum robot (fsdcr) with motion decoupling capability," *Soft Robotics*, vol. 12, no. 3, pp. 350–363, 2025.
[11] W. Zeng, J. Yan, and S. S. Cheng, "Model-based design optimization for motion decoupling in dual-segment flexible robots," *International Journal of Mechanical Sciences*, vol. 275, p. 109312, 2024.
[12] O. Fischer, Y. Toshimitsu, A. Kazemipour, and R. K. Katzschmann, "Dynamic task space control enables soft manipulators to perform real-world tasks," *Advanced Intelligent Systems*, vol. 5, no. 1, p. 2200024, 2023.
[13] C. T. Yilmaz, C. Watson, T. K. Morimoto, and M. Krstic, "Adaptive model-free disturbance rejection for continuum robots," *Automatica*, vol. 171, p. 111949, 2025.
[14] J. Hu, J. Zhang, Y. Zheng, B. Wang, J. Wu, X. Wang, and Y. Yang, "Hybrid-driven continuum robot with decoupled motion patterns for dexterous manipulation," *IEEE Robotics and Automation Letters*, vol. 9, no. 9, pp. 7437–7444, 2024.
[15] Q. Zhao, S. Wang, J. Hu, H. Liu, and H. K. Chu, "Controller design for a soft continuum robot with concurrent continuous rotation," *IEEE/ASME transactions on mechatronics*, vol. 29, no. 6, pp. 4504–4513, 2024.
[16] M. S. Nazeer, C. Laschi, and E. Falotico, "Soft dagger: Sample-efficient imitation learning for control of soft robots," *Sensors*, vol. 23, no. 19, p. 8278, 2023.
[17] T. G. Thuruthel, E. Falotico, F. Renda, and C. Laschi, "Model-based reinforcement learning for closed-loop dynamic control of soft robotic manipulators," *IEEE Transactions on Robotics*, vol. 35, no. 1, pp. 124–134, 2018.
[18] D. Wei, J. Zhou, Y. Zhu, J. Ma, and S. Ma, "Axis-space framework for cable-driven soft continuum robot control via reinforcement learning," *Communications Engineering*, vol. 2, no. 1, p. 61, 2023.
[19] J. Zhang, Q. Fang, P. Xiang, D. Sun, Y. Xue, R. Jin, K. Qiu, R. Xiong, Y. Wang, and H. Lu, "A survey on design, actuation, modeling, and control of continuum robot," *Cyborg and Bionic Systems*, vol. 2022, p. 9754697, 2022.